



POLITECNICO
MILANO 1863

RE.PUBLIC@POLIMI

Research Publications at Politecnico di Milano

Post-Print

This is the accepted version of:

A. Lavatelli, A. Zaroni, E. Zappa, A. Cigada

On the Design of Force Sensors Based on Frustrated Total Internal Reflection

IEEE Transactions on Instrumentation and Measurement, Vol. 68, N. 10, 8588400, 2019, p. 4065-4074

doi:10.1109/TIM.2018.2885604

The final publication is available at <https://doi.org/10.1109/TIM.2018.2885604>

Access to the published version may require subscription.

When citing this work, cite the original published paper.

© 2019 IEEE. Personal use of this material is permitted. Permission from IEEE must be obtained for all other uses, in any current or future media, including reprinting/republishing this material for advertising or promotional purposes, creating new collective works, for resale or redistribution to servers or lists, or reuse of any copyrighted component of this work in other works.

Permanent link to this version

<http://hdl.handle.net/11311/1121932>

On the Design of Force Sensors Based on Frustrated Total Internal Reflection

Alberto Lavatelli¹, Member, IEEE, Andrea Zanoni, Emanuele Zappa, Member, IEEE, and Alfredo Cigada

Abstract—Frustrated total internal reflection (FTIR) of light is a physical phenomenon which can be used to accomplish several measurement tasks. This paper deals with the design and modeling of pressure field or force sensors based on FTIR. In fact, it is possible to convert the value of contact pressure into a light intensity signal, owing to the frustration of reflection of a dedicated medium. In this sense, it is possible to measure pressure/forces with a camera system or a photosensitive sensor. In this paper, the physical principles of the technique are recalled. Then, an experiment will document the behavior of FTIR at micromechanical level. Consequently, a Greenwood–Williamson (GW) model is proposed as a tool to predict the response of the FTIR-based pressure sensor. Experimental data and uncertainty analysis show that the design methodology is able to predict the behavior of the sensor with an uncertainty that is about $\pm 10\%$ of the actual specimen response, thus providing an effective tool to optimize the FTIR experiments.

Index Terms—Force sensing, frustrated total internal reflection (FTIR), pressure field sensing.

I. INTRODUCTION

PRESSURE field sensing is a complex measurement task which is often needed in the field of mechanical [1] and biomedical engineering [2]. The analysis of measurement science literature reveals the existence of several techniques that are able to measure pressure fields (so that a pressure map is retrieved). The most popular implementations are based on capacitive [3], resistive [4], or thermographic [5] methods. This paper, instead, deals with the exploitation of the frustrated total internal reflection (FTIR) phenomenon [6] as a medium to measure pressure or forces applied to a surface. The methodology is well known in the scientific community [7], and it has been used for several measurement tasks [8]–[12].

Far less attention, however, has been focused on design aspects, particularly on the most important component: the sheet of material separating the test specimen and the medium in which total reflection is occurring. The lack of interest can be partly attributed to the fact that one of the most, if not the most, successful applications of FTIR-based sensors

Manuscript received July 9, 2018; revised September 27, 2018; accepted November 15, 2018. The Associate Editor coordinating the review process was Christoph Baer. (Corresponding author: Alberto Lavatelli.)

A. Lavatelli, E. Zappa, and A. Cigada are with the Department of Mechanical Engineering, Politecnico di Milano, 20133 Milan, Italy (e-mail: alberto.lavatelli@polimi.it; emanuele.zappa@polimi.it; alfredo.cigada@polimi.it).

A. Zanoni is with the Department of Aerospace Science and Technology, Politecnico di Milano, 20133 Milan, Italy (e-mail: andrea.zanoni@polimi.it). Color versions of one or more of the figures in this paper are available online at <http://ieeexplore.ieee.org>.

Digital Object Identifier 10.1109/TIM.2018.2885604

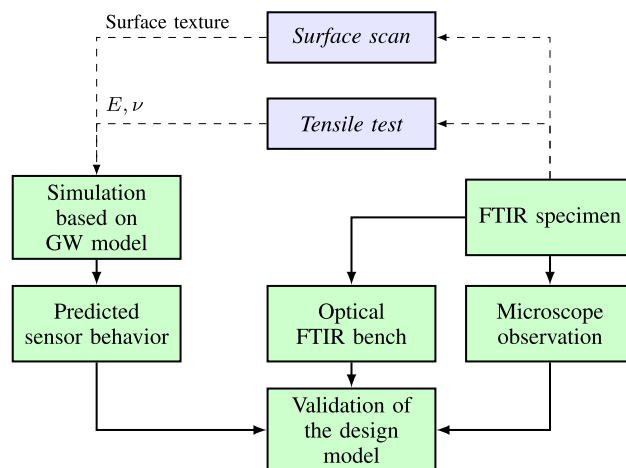


Fig. 1. Structure of the experimental activity.

does not need an interface material at all; FTIR-based sensors are widely used in plantar pressure measuring devices, and as it will become clear in section IV, human skin has ideal characteristics with respect to the FTIR measurements. Up to now, the only publication dealing with the optimization of FTIR test benches is [13].

Consequently, this paper will not present the validation of the measuring technique itself but on the design strategy of FTIR load sensors. The design of FTIR-based sensors is usually done with a heuristic approach, in particular the type of test specimen and its roughness are often selected by means of a trial and error approach. In this paper, on the contrary, we propose a technique to design the force sensors, starting from the mechanical characteristics of the FTIR mediums. The activity is structured as in Fig. 1: an FTIR specimen is selected, and its mechanical properties are estimated through experimental procedures. Then, the sensor output is predicted with a micromechanical model. At the same time, two different experiments are proposed to observe the FTIR behavior. Eventually, the comparison between simulated response and measured one will validate the design approach.

II. FTIR OPERATING PRINCIPLE

A. Frustration of Total Internal Reflection

When an electromagnetic wave traveling into a medium with a refraction index n_1 encounters the surface of separation with a second medium, of refraction index n_2 , it is partly transmitted and partly reflected back [14] (see Fig. 2).

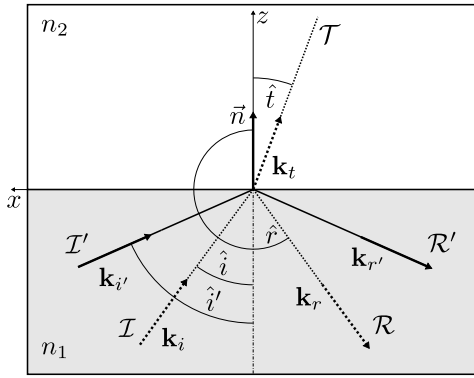


Fig. 2. Refraction of light at the separation interface between two media. The incoming wave \mathcal{I} is partly reflected in the first medium as the wave \mathcal{R} , partly transmitted in the second medium as the wave \mathcal{T} . If the angle of incidence \hat{i} exceeds the critical angle \hat{i}_c , total internal reflection occurs.

Let \vec{n} be the unit vector normal to the plane surface of separation, directed along the positive z axis, and let \mathbf{k}_i be the wave vector of the incident wave, \mathbf{k}_r the wave vector of the reflected wave and \mathbf{k}_t the wave vector of the transmitted wave.

The relationship between the three vectors is found to be [14]

$$\mathbf{k}_i \sin \hat{i} = \mathbf{k}_r \sin \hat{r} = \mathbf{k}_t \sin \hat{t} \quad (1)$$

from which it immediately follows that $\hat{r} = \pi - \hat{i}$ and, taking into account that the frequency of the transmitted wave and that of the incident wave must be equal, i.e., that $k_i/n_1 = k_t/n_2$, results in the well-known Snell's law

$$\sin \hat{i} = \frac{k_t}{k_i} \sin \hat{r} = \frac{n_2}{n_1} \sin \hat{r} \quad (2)$$

from which it is evident that if $n_2 > n_1$, a *critical* angle of incidence \hat{i}_c exists, for which the transmitted wave lies in the $z = 0$ plane

$$\hat{i}_c = \arcsin\left(\frac{n_2}{n_1}\right). \quad (3)$$

Combining Snell's law with the boundary conditions of the magnetic and electric fields at the interface, the so-called *Fresnel coefficients*, relating the amplitudes of the reflected (\mathcal{R}) and transmitted (\mathcal{T}) waves to that of the incident wave (\mathcal{I}), the following is obtained [14]:

$$R_{\perp} = \frac{\mathcal{R}}{\mathcal{I}} = \frac{n_1 \cos \hat{i} - n_2 \cos \hat{t}}{n_1 \cos \hat{i} + n_2 \cos \hat{t}} \quad (4a)$$

$$T_{\perp} = \frac{\mathcal{T}}{\mathcal{I}} = \frac{2n_2 \cos \hat{i}}{n_1 \cos \hat{i} + n_2 \cos \hat{t}} \quad (4b)$$

For incidence angles greater than \hat{i}_c , no real solution exists for Snell's law. In this case, the refraction angle \hat{t} assumes complex values and total internal reflection occurs. Both R_{\perp} and T_{\perp} are complex, and the modulus of R_{\perp} goes to unity. However, the transmission coefficient is not null. In fact,

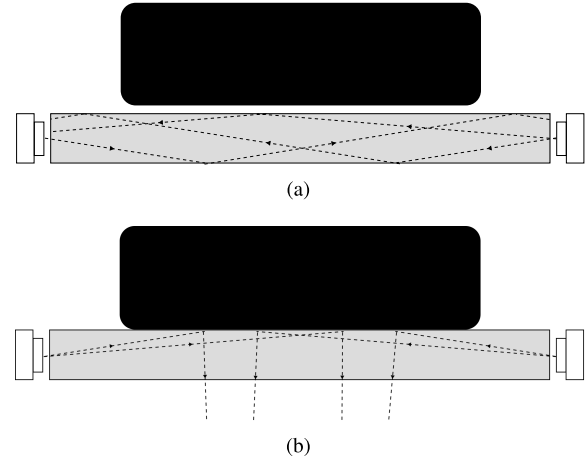


Fig. 3. If a transparent plate is illuminated by the sides, in order for light to produce total internal reflection, an evanescent wave is present at the interface between the plate and the air. If a third medium (the test specimen) is placed on the plate surface, light can be refracted as to reach the underside of the plate. (a) Total reflection without contact. (b) Frustration of light due to contact with FTIR medium.

if $\sin \hat{i} = (1 + \psi^2)^{1/2}$, then $\cos \hat{i} = \pm i\psi$ and

$$T_{\perp} = \frac{2 \cos \hat{i}}{\cos \hat{i} \pm i n_r \psi} \quad (5)$$

with $n_r = n_2/n_1$. Examining the space dependence of the transmitted wave

$$\begin{aligned} E_y^{\mathcal{T}} &= T_{\perp} \cdot \mathcal{I} \exp(-i(\mathbf{k}_t z \cos \hat{r} + \mathbf{k}_t x \sin \hat{r})) \\ &= T_{\perp} \cdot \mathcal{I} \exp(\mp \mathbf{k}_t z \psi) \exp(-i\mathbf{k}_t x (1 + \psi^2)^{1/2}) \end{aligned} \quad (6)$$

it is possible to recognize its nature. It is, in fact, an *evanescent wave*, as evidenced by amplitude modulating exponential $\exp(-\mathbf{k}_t z \psi)$, taking the negative sign to assure the physical meaning of the solution. The wave is damped in space. The decay distance $1/k\psi = \lambda/2\pi\psi$ depends on the media refraction angles and the wavelength of the incident light wave \mathcal{I} .

When a third medium is present in the region occupied by the evanescent wave (see Fig. 3), the reflection can be *frustrated* and the incident wave can be refracted in such a way as to encounter the first interface at angles no longer exceeding the critical one. This phenomenon goes under the name of FTIR. It is widely exploited in different technological applications [6], such as beam splitters, optical waveguide couplers, spectroscopy, laser resonators [15], optical filter design [16], optical imaging [17], and microscopy [18], [19].

B. Contact of Rough Surfaces

The refracted wave can act as a source of light for digital imaging, focused on the contacting area at the interface between the test specimen and a transparent medium, e.g., a suitable glass or plastic plate; the principle is, for example, exploited in tire contact pressure measurement systems [11], [12], [20], [21]. Since the evanescent wave decay distance is comparable to the wavelength of the light source ($\approx 390\text{--}700$ nm), for contact pressure measurement purposes

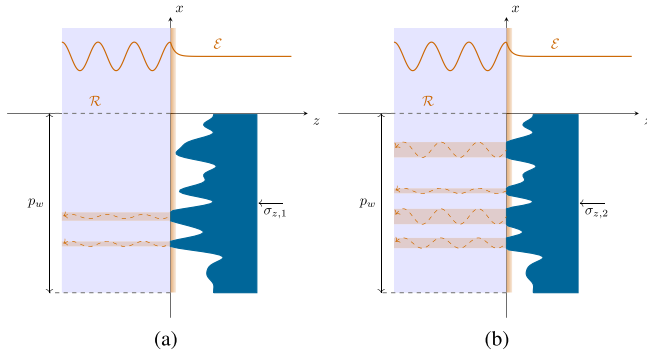


Fig. 4. Effect of superficial roughness on the frustration of internally reflected light. Here, a small portion of the contacting specimen, corresponding to a single pixel in the acquired image, is depicted. In (a), portion is subjected to a normal pressure $\sigma_{z,1}$, while in (b), same portion is subjected to $\sigma_{z,2} > \sigma_{z,1}$. The number of microscopic crests of the material that enter the region of the evanescent wave \mathcal{E} increases and so does the light that reaches the area of the pixel of width p_w .

the assumption that, in all effectiveness, frustration of total internal reflected waves takes place only in actual contacting areas can be made. Viewing the process at the microscopic level, it is also evident how the surface roughness of both media, i.e., the test specimen and the plate, plays a role in determining the amount frustrated light (see Fig. 4). In fact, since the superficial roughness of the glass and that of the specimen are in the μm scale, the progressive increase in microscopic contact areas with the normal pressure (and thus with the deformation of the specimen) is responsible for an increase in brightness in the acquired image. The process can be further stimulated by interposing a thin sheet of compliant material between the specimen and the measuring surface since the ratio between the increase in contact area and the normal pressure applied is proportional to the material mechanical compliance.

C. Observation of FTIR Micromechanics by Means of Total Reflection Microscopy

Even if the macroscopic behavior of FTIR has been observed in several media, the contact micromechanics displayed in Fig. 4 has never been documented as for the authors' knowledge. This step is necessary to claim the chance to use the device as a force sensor. As a consequence, it was necessary to design a test bench dedicated to the observation of the progressive contact of the polymer sheet asperities with the glass medium. The choice has been to observe the contact of the asperities of a polymer sheet (total area is 49.6 mm^2) against a glass surface, owing to a reflection microscope. As shown in Fig. 5(a), an aluminum frame holds a microscope slide glued to the frame itself. The slide is manufactured with high-quality glass, with roughness spanning in the 100-nm range. Consequently, the contact behavior is almost totally due to polymer roughness. The frame has a circular window so that the microscope lens has access to the contact patch. As usual, in reflection microscopy, a narrow-band focused light illuminates the specimen. The polymer specimen lies under the frame that is attached on the other side to another

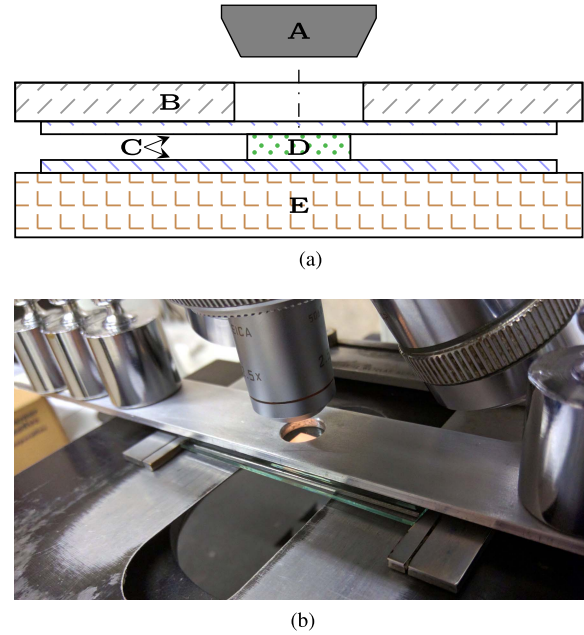


Fig. 5. Optical test bench for the observation of FTIR micromechanics: A—microscope lens, B—aluminum frame, C—microscope slide, D—polymer sheet specimen, and E—slide clamp table. (a) Bench Scheme. (b) System mounted.

microscope slide mounted on a clamp table. The compressive load is provided by the calibrated weights positioned over the aluminum frame, as shown in Fig. 5(b). As the applied load grows, the asperities of the specimen get in contact with the glass of the microscope slide. If the microscope lens is focused on the polymer/glass interface, the contact spots appear darker with respect to the areas in clearance. This phenomenon is exploited to observe the contact micromechanics. With the help of a segmentation algorithm, implemented in a LabView VI, it was possible to find the contact spots and measure each contact area. The ratio between the area of the contact spots and the total image size estimates the ratio C_r between the total contact area and the nominal area of the specimen. In Fig. 6(a), the microscopy image of the contact patch at different levels of loading is presented. In order to assess the scale regularity of the contact micromechanics, the experiment is performed at different magnification levels. It is possible to see that the phenomenon is verified regularly (so that the ratio between total area and contact area holds about constant) at all the different magnification levels, as shown in Fig. 6(b).

III. ANALYTIC ROUGH SURFACES CONTACT MODEL

The objective of this section is to discuss the contact between a random surface and an ideally flat one. Both the surfaces are modeled as hyperelastic solids so that Young's modulus E_1 and E_2 and the Poisson coefficient ν_1 and ν_2 are defined. The solution highlighted in this paper has been formalized by Greenwood and Williamson [22]. The mathematical model proposed by Greenwood and Williamson (GW model) is widely regarded to have fundamental importance in rough contact mechanics, and, although mature and simplified, it suits the analysis of FTIR phenomena. In particular,

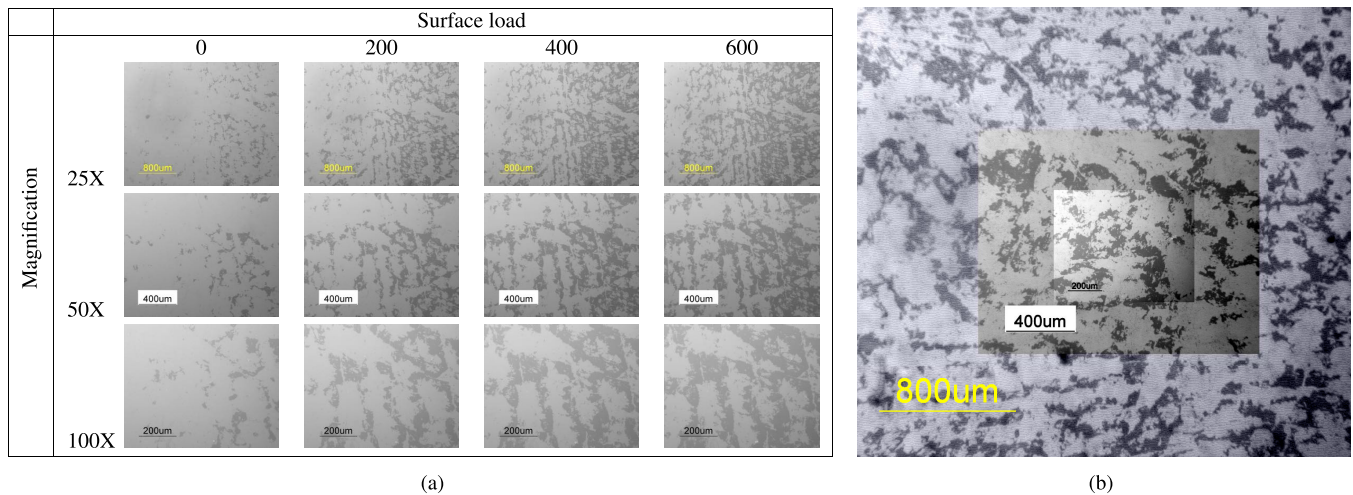


Fig. 6. Microscopy observation of FTIR micromechanics with the test procedure highlighted in Fig. 5. (a) Roughness peaks at contact at different level of load (in grams) and magnification. (b) Nested portrait of the magnification.

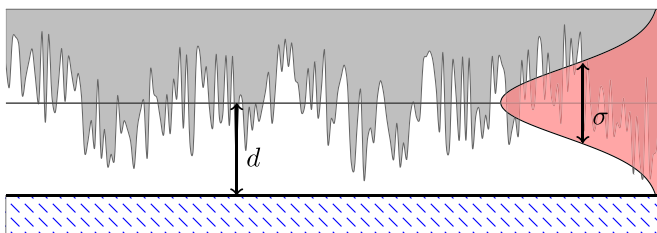


Fig. 7. Monodimensional scheme for the analysis of rough contact micromechanics.

the model has been successfully tested in the description of the rough contact between flat glass surfaces and thin polymer films in [23]. However, the underlying hypothesis entails some limitations in the ability to represent the actual behavior of rough contacts. A deeper discussion about the applicability of the Greenwood models can be found in Section IV-B. In any case, the derivation steps will be recalled in Sections III-B and III-C to provide a better understanding of FTIR.

A. Monodimensional Scheme and Reference System

The problem of computing the contact between the soft medium and the glass is indeed 3-D; however, it can be scaled down to the monodimensional level by considering transverse sections of the two surfaces (see Fig. 7). The rough surface is characterized by a random distribution of asperity heights having standard deviation equal to σ . The reference system in which the problem will be solved is placed on the midline of the asperity heights of the rough surface. The global contact kinematics will be evaluated from the distance d between the midline datum plane and the flat surface. This mid-plane datum is attached to the rough surface, and it is computed in the undeformed configuration. The surface is modeled as a population of asperities \mathbf{a}_k settled at height z_k with respect to the mid-plane datum, as shown in Fig. 8. The asperities are characterized by having a uniform curvature radius β , and

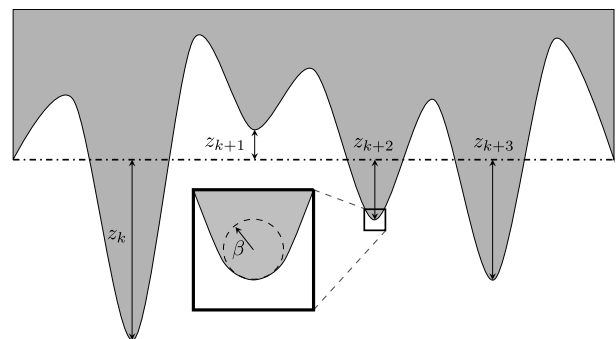


Fig. 8. Geometry description of the surface asperity. The mid-plane datum is indicated in dashed-dotted line.

they are uniformly distributed along the area of the contact patch A_0 . In this way, it is possible to define a constant surface density η so that the total number of asperities N of the contact patch can be expressed in the following equation:

$$N = \eta \cdot A_0. \quad (7)$$

Asperities are modeled as ideal hyperelastic, isotropic, and homogeneous spheres. Consequently, surface roughness is represented as a population of spheres placed at random heights with respect to the surface mid-plane datum. The reference framework is described in Fig. 9.

B. Contact of the Single Asperity

Let us consider the contact behavior of the single asperity \mathbf{A}_k having height z_k . Supposing a Hertzian contact, the asperity is modeled as a sphere having radius equal to β . As a first step, it is possible to evaluate the penetration w [see Fig. 9(b)] of the asperity into the flat surface from the kinematic variable d

$$w = z_k - d. \quad (8)$$

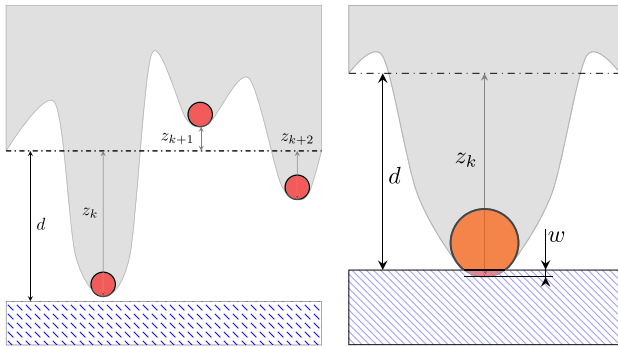


Fig. 9. Description of the mathematical model proposed by Greenwood and Williamson. (a) Representation of rough surface asperities as a set of spheres. (b) Hertzian contact kinematics for the single sphere.

Given w , it is possible to calculate the contact area A_k [24] and the contact load (the force applied to the asperity) P_k

$$\begin{cases} A_k = \pi \beta \cdot w = \pi \beta \cdot (z_k - d) \\ E' = \left(\frac{1 - \nu_1^2}{E_1} + \frac{1 - \nu_2^2}{E_2} \right)^{-1} \\ P_k = \frac{4}{3} E' \cdot \sqrt{\beta \cdot w^3} = \frac{4}{3} E' \cdot \sqrt{\beta \cdot (z_k - d)^3}. \end{cases} \quad (9)$$

C. Statistical Contact Mechanics for the Whole Surface

The previous analysis for the single asperity can be generalized to the whole surface if a probability density function (pdf) of the asperity height $\phi(z)$ is available [25]. In this way, the probability \tilde{p}_k of finding an asperity having height between z_k and $z_k + dz$ can be expressed as

$$\tilde{p}_k = \phi(z) dz. \quad (10)$$

As a consequence, it is possible to calculate the probability \mathbf{P}_d of picking from the whole population of asperities an asperity which is contact with the flat surface

$$\mathbf{P}_d = \int_d^\infty \phi(z) dz. \quad (11)$$

Directly from \mathbf{P}_d , it is possible to calculate the expected value n of contact spots (in other words, the total number of asperities in A_0 which are in contact with the flat surface)

$$n = N \cdot \mathbf{P}_d = N \int_d^\infty \phi(z) dz. \quad (12)$$

The statistical analysis allows to generalize the mechanical quantities A_k and P_k computed for the single asperity. In fact, the expected value F of the quantity $f(z)$ sampled from ϕ_z along the whole contact patch can be computed with the following equation:

$$F = \int_d^\infty f(z) \phi(z) dz. \quad (13)$$

Therefore, proceeding with the calculation, owing to (9), it is possible to compute the effective contact area A

$$A = \int_d^\infty \pi \beta w \cdot \phi(z) dz = \int_d^\infty \pi \beta (z - d) \cdot \phi(z) dz. \quad (14)$$

TABLE I
VALUES OF THE MECHANICAL CONTACT VARIABLES FOR GW MODEL

Property	Symbol	Formula
# contact spots	n	$\eta A_0 \cdot \mathcal{F}_0$
Contact area	A	$\pi \beta \eta A_0 \cdot \sigma \mathcal{F}_1$
Surface load	P	$\frac{4}{3} E' \eta A_0 \beta^{\frac{1}{2}} \cdot \sigma^{\frac{3}{2}} \mathcal{F}_3$

In addition, the total load acting on the contact patch P

$$\begin{aligned} P &= \int_d^\infty \frac{4}{3} E' \cdot \sqrt{\beta \cdot w^3} \cdot \phi(z) dz \\ &= \int_d^\infty \frac{4}{3} E' \cdot \sqrt{\beta \cdot (z - d)^3} \cdot \phi(z) dz. \end{aligned} \quad (15)$$

Previous formulas can be conveniently summarized by normalizing the statistic integrals. In particular, it is convenient to standardize ϕ_z as follows:

$$\begin{cases} s = \frac{z}{\sigma} \\ \varphi(s) = \frac{\phi(z)}{\sigma}. \end{cases} \quad (16)$$

Second, it is possible to normalize the surface distance introducing the standardized displacement h

$$h = \frac{d}{\sigma}. \quad (17)$$

Now, it is possible to define the Greenwood coefficient \mathcal{F}_n of order n , as in the following formula [25]:

$$\mathcal{F}_n = \int_h^\infty (s - h)^n \varphi(s) ds. \quad (18)$$

In this way, the expected values of the mechanical quantities can be expressed as the multiplication of some physical constants by a Greenwood coefficient of order n . The expressions for the main contact calculation results are reported in Table I.

IV. GENERALIZED FTIR-BASED SENSOR MODEL

A. Implementation Notes

The Greenwood model can be easily implemented in numeric analysis environments, such as OCTAVE/MATLAB. The starting point is to have a reliable roughness profile $z_k(x_k)$ sampled with good resolution (such that $\beta \gg x_{k+1} - x_k \forall k : 1 < k < N_p$) and a good number of points (e.g., ISO 3274 [26] requires minimum sampling pitch of $0.5 \mu\text{m}$ and prescribes evaluation lengths that change depending on the expected roughness; in most of the cases, this results in $N_p > 10^3$).

In this way, the steps to compute the contact model are simple. They are summarized in Algorithm 1. For sure, it is necessary to implement the function `greenwood_Fn` that computes the Greenwood coefficients from the standardized pdf of asperity heights. However, this is quite simple when $z_k(x_k)$ is sampled accurately with a good number of points. In this case, the histogram vector is generally smooth; hence, the integration tasks can be carried out through a generic trapezoidal integration scheme. When sampling is poorer, conversely, the numerical integration should be done after the robust probability kernel estimation.

Algorithm 1 Contact Computation

```

1:  $z_k(x_k)$  {Load roughness profile}
2:  $\sigma = \text{std}(z_k)$  {Calculate std. deviation}
3:  $N_p = \text{length}(z_k)$  {Get number of samples}
4:  $e_k = e_1 : \Delta e : e_2$  {Create a PDF computation edge vector
   with  $\Delta e$  spacing}
5:  $\phi(x) = \text{histcounts}(z_k, e_k) ./ (N_p \cdot \Delta e)$  {Calculate height
   PDF}
6:  $\varphi(s) = \phi / \sigma$  {Normalize PDF}
7:  $d = d_1 : \Delta d : d_2$  {Create a compliance vector}
8: for  $i = 1 : \text{length}(d)$  do
9:    $h = d(i) / \sigma$ 
10:  {Compute Greenwood coefficient}
11:   $\mathcal{F}_0 = \text{greenwood\_Fn}(0, \varphi(s), h)$ 
12:   $\mathcal{F}_1 = \text{greenwood\_Fn}(1, \varphi(s), h)$ 
13:   $\mathcal{F}_{\frac{3}{2}} = \text{greenwood\_Fn}(1.5, \varphi(s), h)$ 
14:  {Compute contact area}
15:   $A(i) = \pi \beta \eta A_0 \cdot \sigma \mathcal{F}_1$ 
16:  {Compute contact load}
17:   $P(i) = \frac{4}{3} E' \eta A_0 \beta^{\frac{1}{2}} \cdot \sigma^{\frac{3}{2}} \mathcal{F}_{\frac{3}{2}}$ 
18: end for
19:  $C_r = A / A_0$  {Compute contact area ratio}

```

B. Limitations

The Greenwood model handles contact in a somewhat *naive* manner. As shown in Fig. 9(a), the rough surface is treated as a population of homogeneous spheres of radius β , whose center is randomly positioned in space. This assumption represents a simplifying hypothesis since a set of physical evidences about the geometry of actual rough surfaces and the real interaction among surfaces cannot be represented by the Greenwood model. More in details, the most critical aspects of the Greenwood model have been listed by the author himself in [27].

- Asperities do not exist on real surfaces. Instead, roughness consists of “protuberances on protuberances on protuberances,” since the structure of real surfaces is actually best described as a fractal geometry.
- The spheres used by Greenwood to model the contact do not interact with one another. It means that if the rough surface is moved toward a point where all the protuberances should be squeezed down to the flat surface, it should be verified that $A = A_0$. However, this condition is not modeled by Greenwood; consequently, the spheres can be squeezed to infinity. Eventually, the imposition of very high loads results in $A/A_0 > 1$ as a result of the computation, which is a condition not compatible with the physics of the problem.
- The model handles contact in a linear hyperelastic manner (pure Hooke law); as a consequence, it is impossible to represent the plastic behavior of the surfaces. Furthermore, when plasticity arises during contact, the geometry of the surfaces is permanently altered; hence, contact mechanics depends on the history of the load, a parameter not considered in the model.

- The hypothesis that states that the contact asperities have constant radius is convenient since no particular advantage is gained by adopting more complex geometries, e.g., ellipsoidal. Nonetheless, it reflects the characteristics of rough surfaces generated by means of conventional machining (grinding, milling, and so on) where the roughness profile is determined mainly by the choice of the tool. However, this limits the fields of application of this contact models since, generally, the asperity radius is not constant.

Despite of all the above-listed limitations, Greenwood models spread widely throughout the scientific community as well as the industrial research field. In fact, even if more accurate models of contact micromechanics have been formulated, the family of Greenwood models is the most used due to its straightforward implementation and relatively simple computation. A lot have been discussed about the physical validity of Greenwood models. At the microlevel, the fractal nature of real surface partially rejects the fundamental hypothesis of the Greenwood models. At the same time, the behavior of macroparameters (such as loads or contact area) is well reproduced. The apparent paradox has found a widely accepted solution in the work of Ciavarella *et al.* [28], [29], where the present knowledge about fractal surfaces and the microscopic nature of contact has been used to understand this issue and revitalize the Greenwood models.

C. A/A_0 Factor

In FTIR optics, the transmission of light is proportional to the area ratio C_r

$$C_r = \frac{A}{A_0} = \pi \beta \eta \cdot \sigma \mathcal{F}_1. \quad (19)$$

Now, we want to express C_r as a function of nominal contact pressure p_0 . The first step is to express p_0

$$p_0 = \frac{P}{A_0} = \frac{4}{3} E' \eta \beta^{\frac{1}{2}} \cdot \sigma^{\frac{3}{2}} \mathcal{F}_{\frac{3}{2}}. \quad (20)$$

The ratio between the light transmission coefficient and the nominal contact pressure is

$$\frac{C_r}{p_0} = \frac{\pi \beta \eta \cdot \sigma \mathcal{F}_1}{\frac{4}{3} E' \eta \beta^{\frac{1}{2}} \cdot \sigma^{\frac{3}{2}} \mathcal{F}_{\frac{3}{2}}} = \frac{3}{4} \frac{\pi}{E'} \sqrt{\frac{\beta}{\sigma}} \frac{\mathcal{F}_1}{\mathcal{F}_{\frac{3}{2}}}. \quad (21)$$

In order to derive the mechanical factors that determine the sensitivity of C_r , it is possible to choose an exponential distribution of asperity heights so that $\varphi(s) = e^{-s}$. In this way, the Greenwood factors become

$$\mathcal{F}_n = n! \cdot e^{-h} \rightarrow \begin{cases} \mathcal{F}_1 = e^{-h} \\ \mathcal{F}_{\frac{3}{2}} = \frac{3}{4} \sqrt{\pi} e^{-h}. \end{cases} \quad (22)$$

The previous is derived, owing to the gamma function [30], since $n! = \Gamma(n+1)$ for each $n \in \mathbb{R}$. By substituting (22) in (21), it is possible to compute the contact area ratio as a function of surface load

$$C_r = \frac{\sqrt{\pi}}{E'} \cdot \sqrt{\frac{\beta}{\sigma}} \cdot p_0. \quad (23)$$

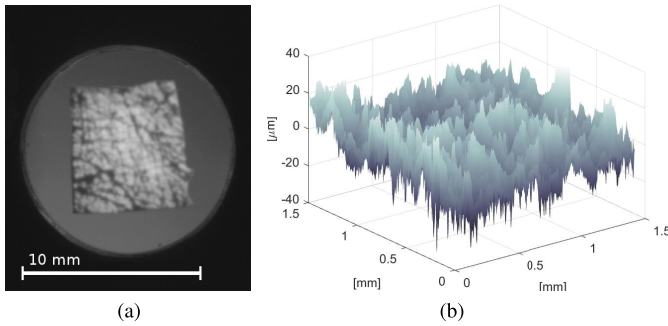


Fig. 10. Silicone film specimen used for model validation purposes. (a) FTIR bench image. (b) Surface scanner output.

Even if retrieved for a simple and particular distribution of asperity heights, (23) highlights the sensitivity driving factors. As predictable, the softer the equivalent modulus E' , the higher the measurement sensitivity. Less intuitively, the sensitivity is driven by the ratio between asperity radius β and standard deviation of asperity height σ . High-performance materials are characterized by asperities well aligned with the medium datum, with respect to their characteristic size (in this conditions, $\sigma \ll \beta$). This explains why human skin outperforms most of the available FTIR media: a very low Young's modulus [31] is coupled with well-aligned friction ridges [32] ($\sigma \approx 8 \mu\text{m}$ and $\beta \approx 400 \mu\text{m}$).

V. MODEL VALIDATION AND UNCERTAINTY ESTIMATION

The specimen used during the microscope experiments documented in Section II-C will also take part in the validation of the proposed model. This choice leads to a multiple check validation: the variation of contact area ratio C_r as a function of applied compression force P predicted by the model is compared to the microscope data and the FTIR optical bench measurement. An image of the specimen under the FTIR bench is displayed in Fig. 10(a). It is possible to observe wrinkles on the surface of the specimen. This has been achieved by treating a silicone film with sandpaper. This has been done on purpose to enhance the sensitivity of the medium, given that it was necessary to work with relatively low-load forces to ensure safe operations of the microscope table.

A. Parameters Estimation

As a first step, it was necessary to qualify the elastic properties of the FTIR medium material according to the ASTM-D882 standard [33]. To do so, 10 specimens (width 20 mm and thickness 1.5 mm) were prepared and, then, tested on an MTS Synergie 200 axial loading machine (whose load cell is calibrated internally according to the ISO 9001 procedures by a secondary sample HBM load cell, certified by the Italian National Institute of Metrology Research). The measured elastic modulus E_1 is equal to 4640(220) kPa and the Poisson ratio ν_1 is equal to 0.39 ± 0.02 . The latter has been evaluated using the Digital Image Correlation. The uncertainty of mechanical parameters is evaluated as the experimental standard deviation of the mean for the 20 samples. This is done

according to the Type-A uncertainty evaluation as formulated in section 4.2 of ISO-GUM 98-3:2008.

Second, it was necessary to retrieve the roughness profile and surface characteristics parameters β and η . To accomplish the task, the surface has been scanned with the Mahr MarSurf CWM 100 machine: a precision, computer-controlled optical measuring instrument with subnanometer resolution. Then, the scanned surface has been processed in order to retrieve the Greenwood parameters using the methodologies highlighted in [34] and [35]. The values of the surface properties computed for the specimen are $\beta = 207 \mu\text{m}$ and $\eta = 279 \text{mm}^2$ (peaks per m^2). The texture of the surface is measured with a resolution in height of 1 nm. Resolution in transverse direction is $2 \mu\text{m}$. For what concerns the purpose of this paper, the surface roughness parameters are managed as fixed constants without uncertainty. This choice is justified by observing that the measurement uncertainty of mechanical parameters of the silicon rubber is much bigger than the uncertainty associated with surface scan data.

From the metrologic traceability point of view, the surface texture scan machine used in this case study does not have a calibration certificate proving SI standard referability. For this kind of machine, the metrologic standard tests are coded by ISO 25178 [36]. However, it is worth to mention that both the measurement uncertainty and the practical resolution of optical machines, such as the surface scan are task-specific [37], as they depend on the optical and geometric characteristics of the surface. The ISO standard, instead, defines the geometry of a series of test specimens (defined in the ISO 25178-Part 70 [38]) and a variety of tests to be performed with them to check that the machine is performing under acceptable precision—with respect to the standard targets. During installation and maintenance, those tests are performed; however, a calibration certificate is not emitted.

B. Design and Construction of an FTIR Optical Bench

The market offers options to buy the turnkey FTIR optical benches. However, they are designed mostly for orthopedic applications, while a general purpose and more flexible one would suit better the purpose of this experiment. Consequently, a custom one has been designed and, then, manufactured. The design is quite simple [see Fig. 11(a)]: four LED light strips pump light on square glass window of 200-mm length and 10-mm thickness. Frustrated reflection is measured, owing to a CMOS camera AVT Marlin F131B equipped with a 25-mm F1.4 lens. LED lights are controlled by a constant current linear supply (so light is controlled without pulsewidth modulation to avoid flickering). The final product is shown in Fig. 11(b).

For what concerns the properties of the glass of the FTIR test bench, it has been decided to avoid mechanical testing and use reference values from the glass manufacturer; Young's modulus has been set to 69.9 GPa and the Poisson coefficient to 0.21. This choice may be regarded as naive, but considering that the values of elastic modulus of the two contact bodies differ by almost four orders of magnitude, we expect that $E' \approx E_1$. Consequently, the contact behavior (and its

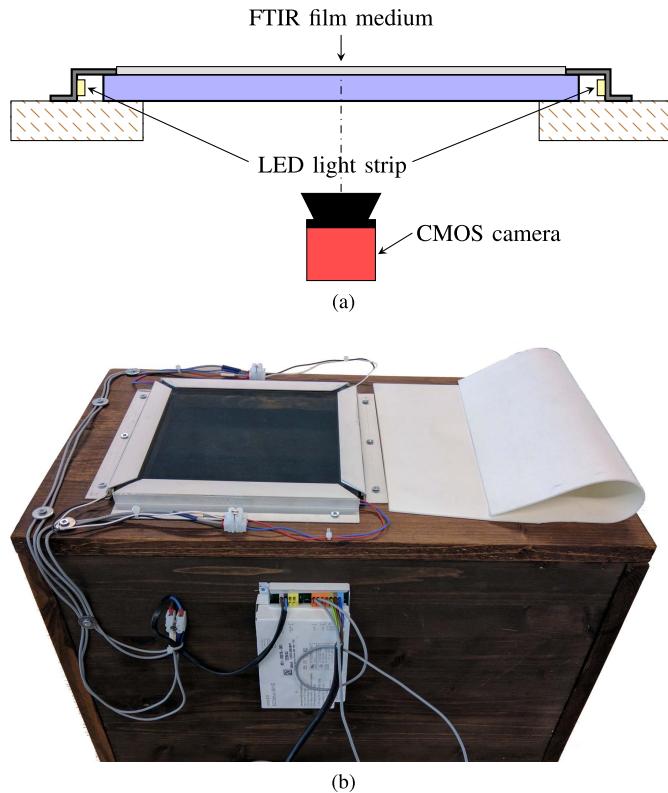


Fig. 11. In-house developed FTIR optical bench. (a) Section of the FTIR optical bench. (b) Picture of the optical bench and the silicon rubber medium.

uncertainty) is mainly ruled by the behavior of the softer medium.

C. Experimental Validation

To validate the model, a simple compression experiment has been set up using the same loading apparatus shown in Fig. 5. The model prediction is tested against the microscope and the optical bench measurements in Fig. 12. As a generic remark, the prediction represents, quite well, the actual behavior of the FTIR patch.

As documented in Section V-A, the mechanical parameters of the FTIR medium are retrieved experimentally, and they are noticeably dispersed around the mean value. Technically, also surface texture is uncertain, but the uncertainty on its parameter is negligible if compared to the scale of roughness due to sandpaper treatment. As a consequence, the only uncertain term of (21) becomes E' . As can be seen in (9), E' depends on both Young's modulus and Poisson's ratio of the polymer strip. Consequently, the final uncertainty of measurement has been evaluated using a Monte Carlo simulation. Given the low number of measurements, the input data are sampled according to a Student's T distribution with 19 degrees of freedom. Contact area ratio confidence bounds are then computed from the 2.5th and 97.5th percentiles after 10^6 realizations of contact behavior (according to the ISO-GUM suggestion). Consequently, the uncertainty bands shown in Fig. 12 are computed without any further hypothesis on the pdf of output data.

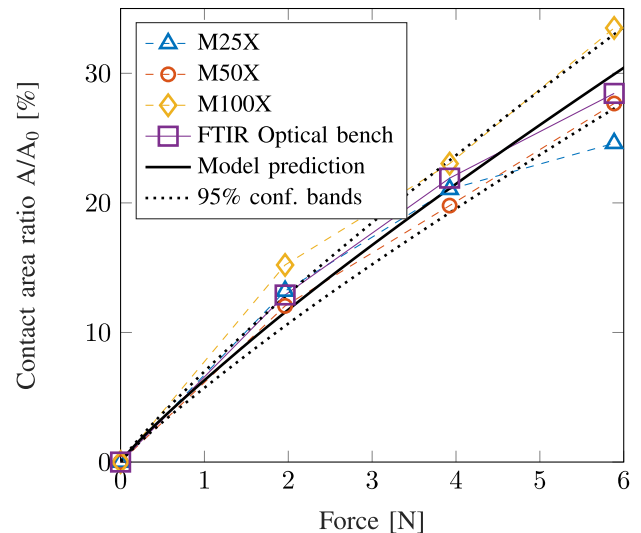


Fig. 12. Model validation plot using the 3-D surface scan data.

The uncertainty bands cover, well, the data. However, at the low levels of compression, the model underestimates the actual contact area ratio. While as the load increases, more accordance is verified within the measured data. This issue is justified by the fractal nature of the contact surface and the necessary filtering required to work with GW models; once the surface is filtered, some asperities are erased, but still they can play a role when load is low enough that they are not completely squeezed.

D. Variability of Model Results by Taking a Simple Roughness Profile

The results commented in Section V-C are computed, owing to a full surface roughness scan. Such an instrument is expensive and not extensively available as roughness meters. Consequently, it is interesting to see how the model behaves if a simple roughness profile is sampled from the FTIR contact patch. Obviously, this adds uncertainty to the estimation of contact parameters; but in authors' opinion, it is still important to address the situation where a popular instrument may be used.

To simulate this situation, 1000 roughness profiles of 3-mm length are extracted from the surface scans. Each roughness profile is identically filtered with an ISO 11562 compliant robust Gaussian filter (waviness + roughness), 2.5-mm cut-off (as recommended by ISO 4288 [39]), and processed to extract GW parameters. Then, mechanical contact is computed using the GW theory. Eventually, for each roughness profile, a realization of the contact behavior is retrieved. Hence, it was possible to compute the mean value and confidence bands in Fig. 13. As can be seen, exploiting a single roughness profile to estimate the behavior of a full contact patch leads to a greater dispersion of results. In fact, the single profile may be extracted from a region of the surface which is less homogeneous with respect to the average surface geometry of the contact patch. As a consequence, the output of this design procedure is more variable than the previous one in Fig. 12. However, the confidence bands highlight that the estimation

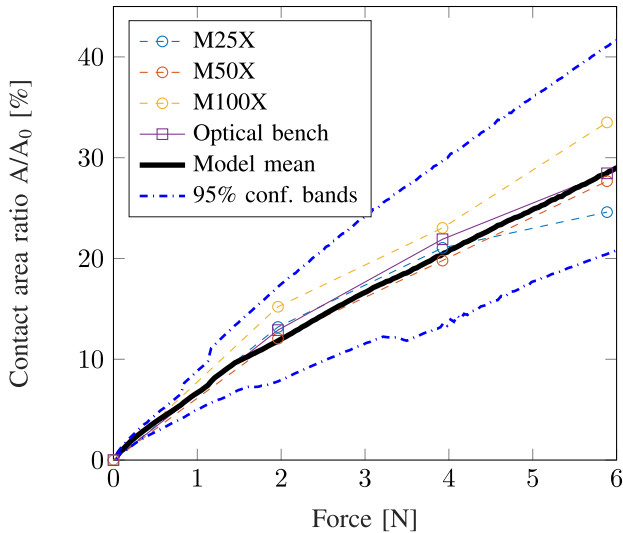


Fig. 13. Model uncertainty plot using single roughness profiles.

region always incorporates the actual measurements. This suggests that the GW model fed by simple roughness profile data is still a viable way to provide a coarse estimation of the parameters for an FTIR experiment. At the same time, since the mean value still resembles data, then it is possible to improve accuracy by averaging results.

E. FTIR Performances and Other Techniques

Considering the two design approaches presented in this paper, it is possible to predict the FTIR medium performances with an uncertainty of about 12% of the measured output when dealing with surface scan and about 30% if the same is done with a single roughness profiles. Necessarily, this is a performance prediction uncertainty, which does not represent the measurement uncertainty of a calibrated FTIR sensor. In this view, the uncertainty linked to the simulations should be interpreted as an uncertainty on the design parameters rather than the uncertainty of the final sensor.

A calibrated FTIR medium, as shown, for example, in [11] and [13], can perform pressure measurements with an uncertainty with respect to the full scale of $1/255$ ($\approx 0.4\%$) when 8-bit images are acquired or $1/1023$ ($\approx 0.09\%$) of the full scale when 10-bit resolution is available, as it is usually the case with digital cameras. The lower value is also typical, for example, of widespread pressure sensing mat systems (see [40]). It is worth noting, though, that while the full scale of such systems is generally fixed by design on a given mat, the maximum pressure that can be measured by an FTIR-based systems depends largely by the interface material saturation characteristics and can, therefore, be tailored to the given application with relative ease. The precision offered by the FTIR systems compares, also favorably, with respect to the systems based on the strain-gage sensorized pins (see [41]) that are characterized typically by uncertainties in the range of 1% of the full scale.

The advantage of FTIR pressure sensing measurement systems with respect to the aforementioned techniques can be

of a greater importance when spatial resolution is taken into account. Very often in practical applications, cameras offering megapixel applications are used to frame target areas with typical major axis dimensions in the range of 0.1 m. The physical area frames by the single pixel are, therefore, in the range of 0.01 mm^2 , as opposed to typical ranges of 1 mm^2 for resistive pressure mat systems and of 50 mm^2 for strain-gage-based systems. It is worth stressing, though, that the actual maximum spatial resolution attainable by FTIR systems depends on the homogeneity of the interface material surface roughness and of its mechanical properties. The theoretical maximum value associated with the pixel framed area can be reached only if the characteristic length of the material inhomogeneities is significantly smaller than the pixel area's edge dimensions.

VI. CONCLUSION

This paper presented the FTIR technique as a viable tool to measure full field contact forces/pressure. The existent literature did not tackle the problem of predicting the behavior (sensitivity, measurement range, and so on) of FTIR systems, given their mechanical parameters. Consequently, the authors proposed a well-known statistic micromechanic model (GW) to simulate the FTIR behavior and then understand what are the main parameters that influence the measurement performances. The approach is validated with two different experimental implementations of FTIR techniques: the classic optical bench and a more accurate reflection microscope setup. Both the experiment demonstrated that a finely tuned model (thanks to highly accurate surface scans) is able to predict the performances of the system with good precision. At the same time, the authors investigated the situation where the model is fed with data coming from a simple roughness profile. In this case, uncertainty arises; however, the result may still be used as a coarse estimation tool.

REFERENCES

- [1] S. Nabulsi, J. F. Sarria, H. Montes, and M. A. Armada, "High-resolution indirect feet-ground interaction measurement for hydraulic-legged robots," *IEEE Trans. Instrum. Meas.*, vol. 58, no. 10, pp. 3396–3404, Oct. 2009.
- [2] S. Nizami, A. Bekele, M. Hozayen, K. J. Greenwood, J. Harrold, and J. R. Green, "Measuring uncertainty during respiratory rate estimation using pressure-sensitive mats," *IEEE Trans. Instrum. Meas.*, vol. 67, no. 7, pp. 1535–1542, Jul. 2018.
- [3] S. Cruz, D. Dias, J. C. Viana, and L. A. Rocha, "Inkjet printed pressure sensing platform for postural imbalance monitoring," *IEEE Trans. Instrum. Meas.*, vol. 64, no. 10, pp. 2813–2820, Oct. 2015.
- [4] A. Kalamdani, C. Messom, and M. Siegel, "Robots with sensitive feet," *IEEE Instrum. Meas. Mag.*, vol. 10, no. 5, pp. 46–53, Oct. 2007.
- [5] M. Tarabini, B. Saggin, D. Scaccabarozzi, and G. Lanfranchi, "Estimation of the orthosis-limb contact pressure through thermal imaging," in *Proc. IEEE Int. Instrum. Meas. Technol. Conf. (I2MTC)*, May 2012, pp. 2733–2737.
- [6] S. Zhu, A. W. Yu, D. Hawley, and R. Roy, "Frustrated total internal reflection: A demonstration and review," *Amer. J. Phys.*, vol. 54, no. 7, pp. 601–607, 1986.
- [7] R. P. Betts, T. Duckworth, I. G. Austin, S. P. Crocker, and S. Moore, "Critical light reflection at a plastic/glass interface and its application to foot pressure measurements," *J. Med. Eng. Technol.*, vol. 4, no. 3, pp. 136–142, 1980.
- [8] M. Shirota, M. A. J. van Limbeek, D. Lohse, and C. Sun, "Measuring thin films using quantitative frustrated total internal reflection (FTIR)," *Eur. Phys. J. E*, vol. 40, no. 5, p. 54, 2017.

- [9] M. Becchetti, R. Marsili, F. Cannella, and A. Garinei, "A new system for the measurement of gripping force based on scattering," *Acta IMEKO*, vol. 6, no. 4, pp. 100–104, 2017.
- [10] R. P. Betts and T. Duckworth, "A device for measuring plantar pressures under the sole of the foot," *Eng. Med.*, vol. 7, no. 4, pp. 223–228, 1978.
- [11] J. Castillo, A. P. D. L. Blanca, J. A. Cabrera, and A. Simón, "An optical tire contact pressure test bench," *Vehicle Syst. Dyn.*, vol. 44, no. 3, pp. 207–221, 2006.
- [12] A. Zanoni, D. Sabato, and F. Cheli, "Validation of a frustrated total internal reflection test bench for tire footprint pressure measurement," in *Proc. 33rd Annu. Meeting Conf. Tire Sci. Technol.*, Cleveland, OH, USA, Sep. 2014, pp. 1–10.
- [13] J. J. C. Aguilar, J. A. C. Carrillo, A. J. G. Fernández, and S. P. Pozo, "Optimization of an optical test bench for tire properties measurement and tread defects characterization," *Sensors*, vol. 17, no. 4, p. 707, 2017.
- [14] A. Lipson, S. G. Lipson, and H. Lipson, *Optical Physics*, 4th ed. Cambridge, U.K.: Cambridge Univ. Press, 2010.
- [15] I. N. Court and F. K. von Willisen, "Frustrated total internal reflection and application of its principle to laser cavity design," *Appl. Opt.*, vol. 3, no. 6, pp. 719–726, 1964.
- [16] G. R. Noyes and P. W. Baumeister, "Analysis of a modified frustrated total reflection filter," *Appl. Opt.*, vol. 6, no. 3, pp. 355–356, 1967.
- [17] O. Bryngdahl, "Evanescent waves in optical imaging," *Prog. Opt.*, vol. 11, pp. 167–221, Jan. 1973, doi: 10.1016/S0079-6638(08)70136-7.
- [18] N. F. van Hulst, M. H. P. Moers, O. F. J. Noordman, R. G. Tack, F. B. Segerink, and B. Bölger, "Near-field optical microscope using a silicon-nitride probe," *Appl. Phys. Lett.*, vol. 62, no. 5, pp. 461–463, 1993.
- [19] F. de Fornel, *Evanescent Waves: From Newtonian Optics to Atomic Optics*, 2nd ed. Berlin, Germany: Springer, 2010.
- [20] V. Roth, B. Moore, and J. Turner, "An optical method for normal contact stress measurement with applications to tire-road interaction," in *Proc. SEM*, Jun. 2004, pp. 1–15.
- [21] J. A. Popio *et al.*, "Apparatus and related methods for automatically testing and analyzing tires utilizing a test pod with a slidably movable cover plate and a gray scale normalization technique," U.S. Patent 5777 219, Jul. 7, 1998.
- [22] J. A. Greenwood and J. B. P. Williamson, "Contact of nominally flat surfaces," *Proc. Roy. Soc. London A, Math. Phys. Sci.*, vol. 295, no. 1442, pp. 300–319, 1966.
- [23] I. Nitta, "Measurements of real contact areas using PET films (thickness, 0.9 μm)," *Wear*, vols. 181–183, pp. 844–849, Mar. 1995.
- [24] K. L. Johnson, "Normal contact of elastic solids—Hertz theory," in *Contact Mechanics*. Cambridge, U.K.: Cambridge Univ. Press, 1985, pp. 84–106.
- [25] K. L. Johnson, "Rough surfaces," in *Contact Mechanics*. Cambridge, U.K.: Cambridge Univ. Press, 1985, pp. 397–423.
- [26] *Geometrical Product Specifications (GPS)—Surface Texture: Profile Method—Nominal Characteristics of Contact (Stylus) Instruments*, Standard ISO 3274:1996, International Organization for Standardization, Geneva, Switzerland, Dec. 1996.
- [27] J. A. Greenwood and J. J. Wu, "Surface roughness and contact: An apology," *Meccanica*, vol. 36, no. 6, pp. 617–630, 2001.
- [28] M. Ciavarella, V. Delfino, and G. Demelio, "A 're-vitalized' Greenwood and Williamson model of elastic contact between fractal surfaces," *J. Mech. Phys. Solids*, vol. 54, no. 12, pp. 2569–2591, 2006.
- [29] M. Ciavarella, J. A. Greenwood, and M. Paggi, "Inclusion of 'interaction' in the Greenwood and Williamson contact theory," *Wear*, vol. 265, nos. 5–6, pp. 729–734, 2008.
- [30] M. Hazewinkel, *Encyclopedia of Mathematics*, vol. 4. Dordrecht, The Netherlands: Springer, 1990.
- [31] C. Edwards and R. Marks, "Evaluation of biomechanical properties of human skin," *Clinics Dermatol.*, vol. 13, no. 4, pp. 375–380, Jul./Aug. 1995.
- [32] Y. Wang, D. L. Lau, and L. G. Hassebrook, "Fit-sphere unwrapping and performance analysis of 3D fingerprints," *Appl. Opt.*, vol. 49, pp. 592–600, Feb. 2010.
- [33] *Standard Test Method for Tensile Properties of Thin Plastic Sheeting*, Standard ASTM D882, 2012.
- [34] J. I. McCool, "Relating profile instrument measurements to the functional performance of rough surfaces," *J. Tribol.*, vol. 109, pp. 264–270, Apr. 1987.
- [35] M. Kalin, A. Pogačnik, I. Etsion, and B. Raeymaekers, "Comparing surface topography parameters of rough surfaces obtained with spectral moments and deterministic methods," *Tribol. Int.*, vol. 93, pp. 137–141, Jan. 2016.
- [36] I. O. Aver'yanova, D. Y. Bogomolov, and V. V. Poroshin, "ISO 25178 standard for three-dimensional parametric assessment of surface texture," *Russian Eng. Res.*, vol. 37, pp. 513–516, Jun. 2017.
- [37] G. Moroni, W. P. Syam, and S. Petrò, "A simulation method to estimate task-specific uncertainty in 3D microscopy," *Measurement*, vol. 122, pp. 402–416, Jul. 2018.
- [38] *Geometrical Product Specification (GPS)—Surface Texture: Areal—Part 70: Material Measures*, Standard ISO 25178-70:2014, International Organization for Standardization, Geneva, Switzerland, Feb. 2014.
- [39] *Geometrical Product Specifications (GPS)—Surface Texture: Profile Method—Rules and Procedures for the Assessment of Surface Texture*, Standard ISO 4288:1996, International Organization for Standardization, Geneva, Switzerland, Dec. 1996.
- [40] "Comparison of interface pressure measurement options," Tekscan Inc., Boston, MA, USA, White Paper, Aug. 2008. [Online]. Available: <https://www.raien.com.ar/files/pdf/418/tekscan-uso-industrial-raien.pdf>
- [41] "Force matrix sensor," A&D Technol., Ann Arbor, MI, USA, White Paper, 2011. [Online]. Available: https://aanddtech.com/wp-content/uploads/2018/07/fms_datasheet.pdf



Alberto Lavatelli (M'14) received the M.Sc. degree in mechanical engineering from the Polytechnic University of Milan, Milan, Italy, in 2015, where he is currently pursuing the Ph.D. degree with the Department of Mechanics.

His current research interests include the development of vision-based techniques applied to mechanical and thermal measurements.



Andrea Zanoni received the M.Sc. degree in mechanical engineering and the Ph.D. degree in mechanical system's dynamics with a focus on frustrated total internal reflection measurement systems from the Politecnico di Milano, Milan, Italy, in 2011 and 2015, respectively.

He is currently a Post-Doctoral Research Fellow with the Aerospace Science and Technology Department, Politecnico di Milano. His current research interests include rotorcraft physics-based, pilot-in-the-loop real-time simulation, and bioaeroservoelastic investigation of adverse pilot-rotocraft dynamic interactions.



Emanuele Zappa (M'10) received the Ph.D. degree in applied mechanics from the Politecnico di Milano, Milan, Italy, in 2002.

Since 2001, he has been a Researcher with the Department of Mechanical Engineering, where he is currently an Associate Professor. He is the author of several publications in the field of measurements, with focus on vision-based techniques: digital image correlation, 3-D structured light scanning, and stereoscopy. The original author's contribution covers the development, the improvement, and the uncertainty analysis of the fore mentioned techniques, as well as their application in complex and harsh environments.



Alfredo Cigada received the M.Sc. degree in mechanical engineering and the Ph.D. degree in applied mechanics from the Politecnico di Milano, Milan, Italy, in 1990 and 1994, respectively.

From 2003 to 2008, he was involved in teaching at the University of Pavia, Pavia, Italy. Since 2002, he has been a Professor of mechanical and thermal measurements with the Politecnico di Milano. He is the author of more than 130 papers on the following topics: fluid structure interaction, vehicle substructure interaction, cable vibrations, electromechanical interaction, image processing, new measurement techniques, and new sensors (MEMS and fiber optic sensors), acoustics, structural health monitoring, safety and security, crime fighting, and renewable energy.